Proc. Natl. Acad. Sci. USA
Vol. 81, pp. 6363–6367, October 1984
Biophysics

Radial distributions of density within macromolecular complexes determined from dark-field electron micrographs

(scanning transmission electron microscope/tobacco mosaic virus structure/radiation damage/unstained freeze-dried specimens/digital image processing)

ALASDAIR C. STEVEN*†, JAMES F. HAINFELD‡, BENES L. TRUS§, PETER M. STEINERT¶, AND JOSEPH S. WALL‡

*Laboratory of Physical Biology, National Institute of Arthritis, Diabetes and Digestive and Kidney Diseases, National Institutes of Health, Bethesda, MD 20205; ‡Biology Department, Brookhaven National Laboratory, Upton, NY 11973; §Computer Systems Laboratory, Division of Computer Research and Technology, National Institutes of Health, Bethesda, MD 20205; and ¶Dermatology Branch, National Cancer Institute, National Institutes of Health, Bethesda, MD 20205

Communicated by Albert V. Crewe, June 28, 1984

ABSTRACT **A procedure has been developed for direct determination of radial distributions of density in filamentous and spheroidal particles by analyzing dark-field scanning transmission electron micrographs of unstained freeze-dried specimens. Unlike electron microscopic methods based on staining or shadowing with heavy atoms, this approach can be used to probe the internal structure of macromolecular complexes. As an experimental proving ground, we have applied the procedure to tobacco mosaic virus (TMV) and to RNA-free helical polymers of TMV coat protein. Both structures are found to project outermost diameters of 17.6 ± 0.4 nm, to have empty axial holes ≈3.5 nm in diameter, and to have density peaks at radii of 2.5 ± 0.5 and 6.7 ± 0.3 nm. Thus visualized, the only significant difference between them is the presence in the virion of an additional density peak at 4.1 ± 0.5 nm contributed by its internalized RNA molecule. We have also used the procedure to monitor the structural expression of radiation damage in the low electron dose regime prior to the onset of significant mass loss. Changes in the radial density profiles are detected at average doses as low as ≈400 electrons per nm^2: the trend is for the internal structure of these particles to fuse toward a state of uniform density, although the values of their outermost diameters remain unaffected.**

Radial profiles of average mass density afford valuable information for mapping the distribution of molecular components in filamentous or spheroidal particles, particularly if the molecular weights and stoichiometries of these constituents are known. Such a profile imposes a constraint to which aspiring topographic models must conform: it may also directly reveal the locations of components of relatively low density (such as lipids) or relatively high density (such as nucleic acids). In this paper, we explore the potentialities for obtaining such profiles by analyzing low-dose electron micrographs of unstained freeze-dried specimens.

The utility of dark-field scanning transmission electron microscopy (STEM) (1) is now well established for determining the masses of isolated particles, the linear densities of filaments, or the mass-per-unit area of membranous specimens (2–4). Here we have aimed to extend this method to characterize the spatial distribution of mass within macromolecular complexes. We present a method for overcoming the limitation of sparse sampling in low-dose STEM images, whereby the electron probe diameter is much smaller than the sampling raster step. This method ("Vernier sampling") re-sorts the scan data to yield optimally averaged transverse mass projections when applied to filamentous or spherical particles. To convert these projections into radial density distributions, we introduce a noniterative real-space algorithm and describe some of its properties, which include certain practical advantages over conventional Fourier–Bessel inversion for handling data of this kind.

As an experimental model system, this approach is applied to particles of tobacco mosaic virus (TMV) and to helical polymers of TMV coat protein assembled in the absence of RNA. Particular attention is paid to the quantitative reproducibility of structural details, to the resolution attained, and to the development of structural damage with increasing levels of electron irradiation. These results are compared with the corresponding density profiles evaluated earlier by x-ray diffraction analysis (5, 6).

EXPERIMENTAL PROCEDURES

Electron Microscopy. Digital STEM images were recorded at the Brookhaven Biotechnology Resource microscope (7) operating at 40 keV. The diameter of its focused electron probe is 0.25 nm and a focused beam was used throughout. The sampling rates used were such that the image fields (512 × 512 pixels) covered areas of 0.27 μm^2 or 1.08 μm^2 at the specimen. The signal from the large-angle dark-field detector, whose collection angle subtends 40–200 mrad (7), was used in all analyses. Specimens were prepared by freeze-drying as described (7) and were maintained at −160°C on a liquid-N_2-cooled stage during observation. Electron doses were normally 100–300 electron/nm^2.

Specimens. Tobacco mosaic virus particles were column-purified by gel filtration on Sephadex G-100 immediately before use to eliminate any degraded or aggregated material. RNA-free helical polymers of TMV coat protein assembled from purified protein according to previously described procedures (8, 9) were kindly provided by T. Schuster and M. Adams (University of Connecticut, Storrs, CT).

Image Processing. Except as specified below, image processing was carried out using the PIC system (10), an integrated package of subroutines adapted in part from the earlier MDPP system (11). This program was run interactively on a DEC VAX 11/780 computer, also using a DeAnza IP8500 video frame buffer, a Matrix 4007 camera station, and a Perkin Elmer 1010G for high-resolution film writing. Analysis and graphics of one-dimensional traces were done using the MLAB program (12), running on a DEC-10 computer.

Vernier Sampling. To compensate for resolution-limiting effects of sparse Cartesian sampling (the focused beam, 0.25 nm in diameter, sampled the specimen on a square raster at intervals of 1 or 2 nm), the data points were re-sorted by

The publication costs of this article were defrayed in part by page charge payment. This article must therefore be hereby marked "*advertisement*" in accordance with 18 U.S.C. §1734 solely to indicate this fact.

Abbreviations: STEM, scanning transmission electron microscope; TMV, tobacco mosaic virus.

†To whom reprint requests should be addressed at: Bldg. 6, Rm. 114, National Institutes of Health, Bethesda, MD 20205.

directing them parallel to the particle axis into an array of bins (Fig. 1). Averaging the points collected by each bin gives a sampling of the particle's transverse mass projection. Any desired sampling rate may be chosen, and a bin size of 0.33 nm was routinely used in this study.

After display of an image on the video monitor, the angular orientations of designated particle segments (cf. *Results*) were determined by repeated measurements, using a graph-pen and table system. To minimize lateral smearing (with consequent loss of resolution), which would be caused by error in determination of this angle, projections were calculated in the first instance for relatively short segments of particle (on average, 50 nm long). These traces were subsequently aligned and combined by cross-correlation methods (13). Measurements of outermost diameters (defined as the distance between the first points on either side of the particle at which the signal falls to background) were then made from these projections without further processing. Prior to reconstruction of the radial density profile, a further improvement in signal-to-noise was obtained by performing two-fold symmetrization and by imposing a bell-shaped low-pass filter in Fourier space, which had a value of unity out to spatial frequencies of 0.5 nm^{-1}, and a value of zero beyond 0.67 nm^{-1}. Some experimentation was also carried out in varying these limits (cf. *Results*). Finally, a background subtraction was made and the projection was set to zero outside the predetermined edges of the particle.

Reconstruction of Average Radial Density Profiles. To convert the transverse mass projections into radial density distributions, we have derived a noniterative real-space algorithm, which appears to be particularly suitable for this purpose. With cylindrically symmetrical structures considered in cross section, the effect of translational averaging along the particle's axis is equivalent to rotational averaging around its axis. In consequence, the resulting radial density distribution may be considered, in terms of discreet sampling, as a set of concentric annuli, each of thickness Δ and of constant density (Fig. 2). A set of linear equations relates the values of the sampled projection $\{P_n\}$, to the density values within the annuli $\{\rho_n\}$, viz.

$$p_n = f_n^{(n)} \cdot \rho_n \quad [1]$$

$$p_{n-1} = f_n^{(n-1)} \cdot \rho_n + f_{n-1}^{(n-1)} \cdot \rho_{n-1} \quad [2]$$

$$p_{n-2} = f_n^{(n-2)} \cdot \rho_n + f_{n-1}^{(n-2)} \cdot \rho_{n-1} + f_{n-2}^{(n-2)} \cdot \rho_{n-2} \quad [3]$$

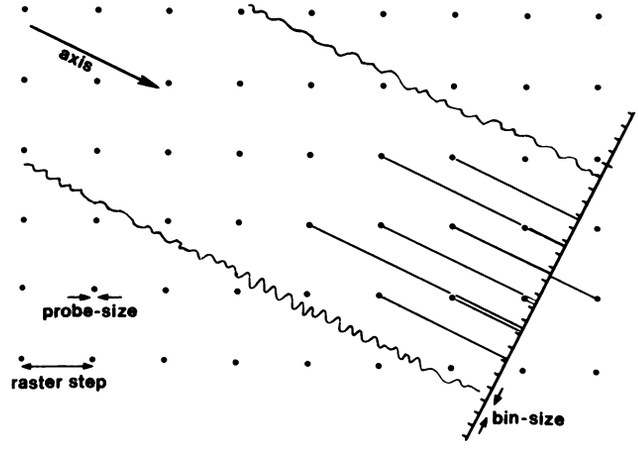

FIG. 1. Principle of Vernier sampling. Sparsely spaced samples obtained with the focused electron probe (dots) are re-sorted computationally by projecting them parallel to the particle axis into a transverse array of bins. The points thus collected are then averaged on a bin-by-bin basis.

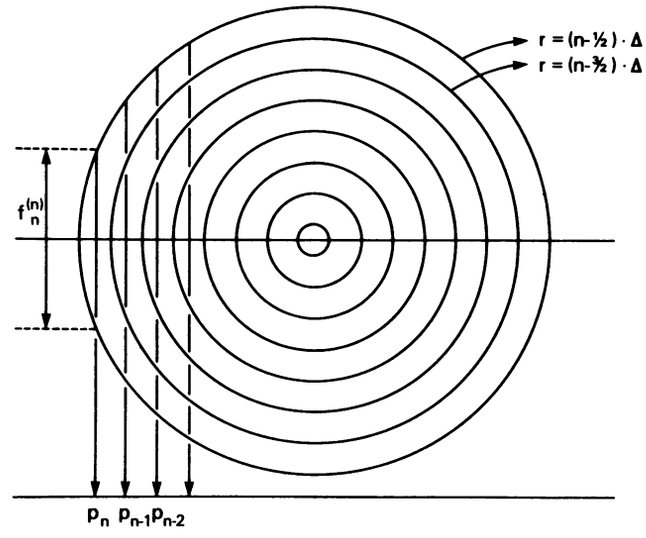

FIG. 2. Cross section of an axially averaged helix, considered as a system of concentric annuli of thickness Δ (apart from the central one: 0.5 Δ). The annuli are sampled by equally spaced projection rays (p_n).

$$p_{n-k} = \sum_{j=0}^{k} f_{n-j}^{(n-k)} \cdot \rho_{n-j} \quad [k]$$

where

$$1/\Delta \cdot f_{n-l}^{(n-k)} = [(2k - 2l + 1)(4n - (2k + 2l + 3))]^{1/2} - [(2k - 2l - 1)(4n - (2k + 2l + 5))]^{1/2}$$

$$\text{for } l = 0, \ldots (k - 1),$$

and

$$1/\Delta \cdot f_{n-k}^{(n-k)} = [4(n - k) - 3]^{1/2}$$

Here, $f_k^{(n)}$ is the length of the intercept of the nth projection ray through the kth annulus, and the thickness of each annulus is Δ. This set of equations is upper-diagonal and, consequently, it may be solved exactly without recourse to iterative methods.

In practical terms, the algorithm has the following useful properties: (*i*) the physical constraint of positive mass density is easily imposed. The incidence of significant regions of "negative density" would, however, be symptomatic of noisy data, or that the assumption of cylindrically symmetric preservation of structure was significantly in error. (*ii*) This procedure is stable in the presence of discontinuities in the density function or its derivatives, which, with Fourier–Bessel inversion methods, can give rise to artifactual fluctuations at such points: thus it "sees edges clearly." (*iii*) The effects of a limited degree of flattening of the particle may be accommodated by substituting appropriate ellipses for circles in Fig. 2, and using a simple modification of the above equations.

For analysis of spherical particles, essentially the same procedure is applicable except that, in calculating the transverse (central) projection of such particles, the array of "collection bins" used to obtain Vernier sampling should, in effect, be rotated around the center of the particle rather than swept along its axis as in the filamentous case.

RESULTS

Radial Distributions of Mass in TMV and Helical Polymers of TMV Coat Protein. Micrographs typical of those analyzed in this study are shown in Fig. 3. The noise levels present in

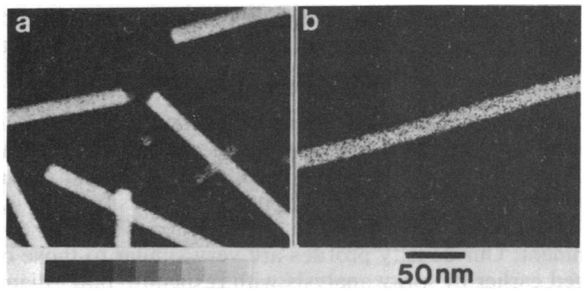

FIG. 3. STEM dark-field micrographs of TMV (*a*) and helical polymer of TMV coat protein (*b*). The specimens are unstained and the highest density features are represented as white. The gray-scale ramp represents density increments of 1.3 kDa/nm^2.

the unprocessed images are appreciable, largely on account of statistical fluctuations caused by the low levels of illumination used: no distinction between the RNA-containing virus particles (Fig. 3*a*) and the protein polymers (Fig. 3*b*) is immediately apparent. Segments of particles chosen for analysis were straight, free of perceptible adsorbed contaminants, and had images that, when viewed at a glancing angle, gave indications of a stripe along the particle center, corresponding to the known central hole of TMV. These images were then processed as described above. The projections shown in Fig. 4 *a* and *b* illustrate the reproducibility attained with individual protein helices, and the corresponding data for virions are shown in Fig. 4 *d* and *e*. The global average projections are compared in Fig. 4 *c* and *f*, where the relative scaling has been performed on the assumption that the mass-per-unit length of the protein polymers is 0.95 that of the virus—i.e., the same apart from the absence of RNA (14). Toward the periphery, the two curves are superimposable (Fig. 4*f*), whereas toward the center, the virion projects significantly higher densities.

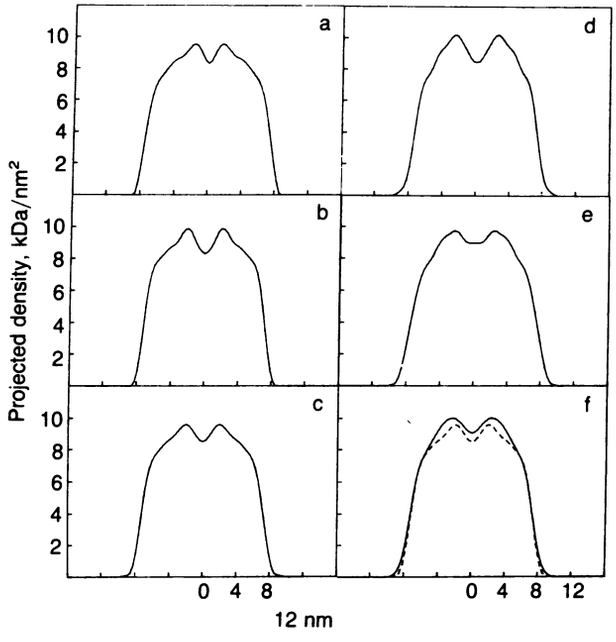

FIG. 4. Transverse mass projections of individual TMV coat protein polymers (*a* and *b*), and of virions (*d* and *e*), calculated from dark-field STEM micrographs. The global average projections are given in *c* and *f*, respectively [*c* is also overlaid in *f* (– – –) to facilitate direct comparison]. Projections *c* and *f* were obtained by combining 24 segments each, amounting to cumulative lengths of 1.47 and 1.48 μm. The individual particle reconstructions (*a*, *b*, *d*, and *e*) represent averages over 3–5 segments, giving cumulative lengths of 0.2–0.3 μm.

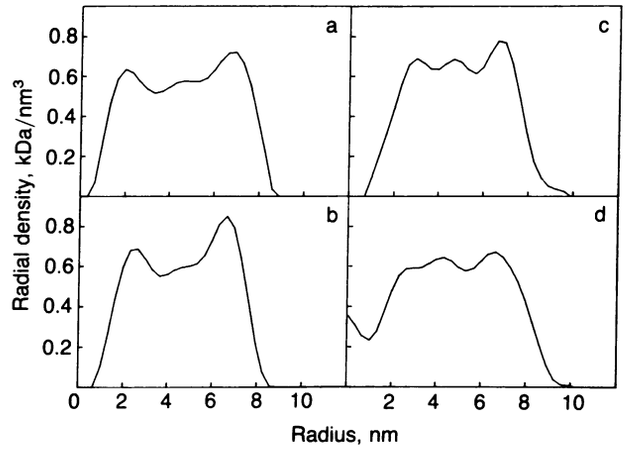

FIG. 5. Radial profiles of average dry density reconstructed from electron micrographs of TMV coat protein helices (*a* and *b*), and virions (*c* and *d*).

The radial density profiles derived from these data are shown in Fig. 5. In both cases, the density level does indeed fall precipitously at the center of the particle. With the protein polymers (Fig. 5 *a* and *b*), we consistently observe a density maximum at a radius of ≈2.5 nm, separated by a trough from a second, somewhat higher, peak at 6.5 nm radius. In the reconstructions of the virus particles (Fig. 5 *c* and *d*), the outermost peak is also present as is the inner ($r \approx 2.5$ nm) peak albeit with somewhat greater variability, but in this case we observe an additional intervening peak at a radius of ≈4 nm. Measurements of the radial positions of these features, together with outer diameter measurements from the unprocessed projections are compiled in Table 1. The global average reconstructions are compared in Fig. 6*a*. In the case of the virion, the two inner peaks resolved in individual reconstructions have coalesced, presumably on account of the somewhat greater variability of visualized detail in this region. On the other hand, the outer peak is in perfect agreement with that recorded for the RNA-free protein polymers. In the difference map (Fig. 6*b*), the only significant feature is a peak of positive density located at a radius of 4 nm. When integrated, this peak accounts for 4.5% of the total mass. For this reason, and because of its radial location, we conclude that this feature represents the packaged RNA molecule.

Resolution and Reproducibility. To assess the effective resolution of the data (i.e., the upper bound of instrumental resolution and of the level to which molecular structure has survived specimen preparation and electron microscopic observation), we used two approaches. First, in processing the averaged projection data prior to reconstruction, a gradually increasing series of band-limiting cutoffs was applied. In each case, the reproducibility of the features present in the resulting reconstruction was appraised. By this criterion, we concluded that a spatial frequency cutoff between 1.5 nm^{-1} and 2.0 nm^{-1} amounted to the highest resolution, which yielded essentially the same features. Second, we evaluated equatorial diffraction patterns to determine the highest spatial frequency at which the structure factor remained above

Table 1. Radial positions (nm) of density peaks

	Outermost diameter, nm	Peak 1	Peak 2	Peak 3
Virion (n = 7)	17.6 ± 0.4	2.5 ± 0.5	4.1 ± 0.5	6.7 ± 0.2
Coat protein helix (n = 8)	17.9 ± 0.7	2.6 ± 0.6	—	6.8 ± 0.5

Peaks 1 and 2 were clearly resolved in 5/7 individual virion reconstructions. The quoted uncertainties are standard deviations.

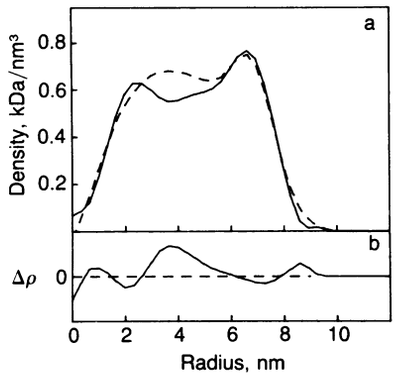

FIG. 6. (*a*) Comparison between radial profiles of average dry density of TMV coat protein helices (solid line) and virions (long dashes), derived from the projections shown in Fig. 4 *c* and *f*. (*b*) The difference curve between these traces has a single significant peak of positive density centered at a radius of ≈4 nm.

the noise level. These procedures yielded consistent results.

Systematic Changes in Internal Structure Effected by Protracted Electron Irradiation. We have studied the changes that take place in these radial density profiles over the course of successive scans. In some respects, such data can be more informative about the redistribution of mass within irradiated biological specimens than the conventional method of monitoring the fading of electron diffraction orders from organic crystals, because all diffraction orders do not respond uniformly, and because density profiles are more directly interpretable in terms of structural preservation of individual particles. The results for TMV coat protein helices are summarized in Fig. 7. By applying cross-correlation methods, we were able to ensure that precisely the same portions of particle were compared from successive exposures. Over the entire series, the total mass decreased by a total of ≈3.5%, a rate of mass loss quite consistent with those observed in earlier experiments (3, 4). The systematic trend observed here is the gradual smearing out of all internal features observed in the first scan reconstruction, most particularly the central hole. In other words, after an electron dose of $\approx 10^3$ electrons per nm^2, the internal structure of these particles fuses to a state of approximately uniform density. It

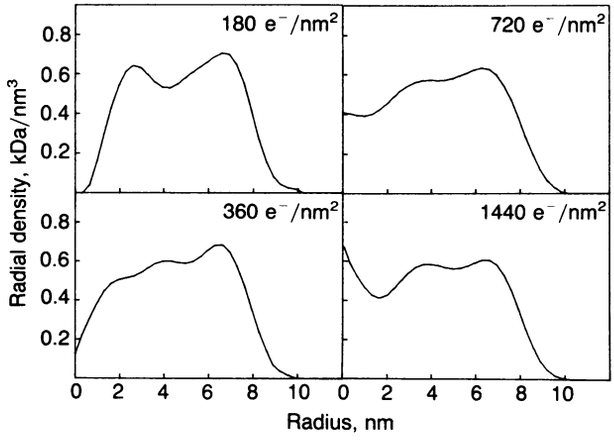

FIG. 7. Sequence of radial density profiles showing successive changes in internal structure undergone by helical polymers of TMV coat protein with increasing levels of electron irradiation. The total particle length averaged was 0.53 μm, and electron counting statistics were the same for each reconstruction. Each image in the series was recorded with an average dose of 180 electrons per nm^2. Thus, for instance, the profile at 720 electrons per nm^2 corresponds to the fourth scan pre-irradiated with 540 electrons per nm^2.

is noteworthy, however, that their outer diameter does not change appreciably over the course of successive exposures.

DISCUSSION

Comparison with X-Ray Fiber Diffraction. The analagous experiments were performed by means of x-ray fiber diffraction of hydrated sols almost 30 years ago by Caspar (5) and Franklin (6), using equatorial diffraction intensities to a cutoff of ≈ 1.0 nm^{-1} and heavy atom derivatives for phase assignment. Our density profiles are very similar to those obtained earlier by x-ray analysis with respect to outer diameter (17.4 nm vs. 16.8 nm), in the existence and extent of the central hole, and in determination of the radial position of the RNA. However, the RNA is visualized as a denser more compact peak in the x-ray profile (5), presumably on account of the higher resolution. One slight difference between the two sets of results concerns the height of the outermost protein peak ($r \approx 6.5$ nm) relative to the others. In the present electron microscopic analysis, this feature has by a slight but consistent margin the highest density, whereas the situation is reversed in the x-ray maps (5, 6), which also resolve two separate peaks in this region. As yet, we have no conclusive explanation for this disparity, but we consider it implausible that it should arise from the difference in resolution. One possible explanation might lie in the different baselines for contrast in the respective methods: viz, density is visualized relative to that of solvent in x-ray diffraction and relative to the vacuum with freeze-dried electron microscopic specimens. Thus, it is to be expected that regions from which water is on average more effectively excluded will tend to appear less dense in the x-ray analysis as compared to the STEM reconstruction. An extreme case would be represented by the hydrophobic phase of a lipid bilayer, which would be represented at or below background density in the x-ray map of a fully hydrated specimen but would be visualized with strong positive contrast by the present method. Thus, the eventuality that the protein at this radial location in the TMV particle has a relatively low degree of hydration—as, in fact, is indicated by recent x-ray diffraction studies (14)—might well account for the differing representations of this region.

Comparison with Negative Staining Results. End-on projections of "disk" aggregates of TMV coat protein stained with heavy metal salts have been examined by Crowther and Amos (15) and by Nonomura and Ohno (16). These authors detected a narrow dark-staining ring at a radius of ≈4 nm, which they interpreted as a stain-penetrable groove to be occupied by the RNA in the assembled virus. Taken alone, their results do not rule out alternative explanations such as positive staining of some locus on the coat protein subunit. The high order of rotational symmetry of the disk would naturally propagate such local stain accumulations into having the appearance of azimuthal continuity. However, despite some discrepancies in dimensions [many of the published images (15) appear to project diameters considerably in excess of 20 nm as opposed to the figure of 17.4 nm obtained here], their final interpretations are generally in line with the present results.

Future Prospects. The most significant aspect of the present results is that they underwrite the feasibility of using dark-field electron microscopy of unstained specimens to determine average radial distributions of density for helical and filamentous as well as for spherical particles. To judge by the reproducibility of details in different reconstructions, the resolution obtained here is at the level of 1.5–2.0 nm. Individual reconstructions involved combining 4–6 segments, corresponding to cumulative particle lengths of 0.2–0.4 μm. The global averages (Fig. 6) both included 25–30 such segments, amounting to 1.5 μm. This amount of averaging is easily handled, even with interactive processing, and

may be substantially increased by implementation of a semi-automatic procedure (unpublished observations).

Comparing successive reconstructions from an exposure series (Fig. 7), we find that significant changes take place even with cumulative electron doses of $\leq 10^3$ electrons per nm^2, which elicit mass loss of only a few percent and leave the outer diameter quite unaffected. A melt-down of internal structure seems to take place, leading to a state of uniform density. This acute sensitivity to beam damage raises the possibility that significant degradation of internal structure may already have been sustained in recording the first scan. In consequence, improved resolution may be contingent on further reduction in electron dose levels.

Preservation of molecular structure upon freeze-drying is another aspect that will require further research. Our empirical observation is that TMV particles in different parts of the same grid exhibit differing states of preservation. We conclude that our freeze-drying process, albeit carried out slowly at a constant sublimation rate and under high vacuum (7), has been more or less efficacious in preserving structure in different parts of the grid. However, freeze-drying quality does not vary randomly from particle to particle; rather, it is locally consistent over areas tens of microns in extent. This consideration suggests that, as a pragmatic and hopefully temporary measure, TMV should be used not only as an internal mass standard, but also as a local quality control when working with an "unknown" specimen.

Thus we conclude that, although this method has much scope for improvement and innovation, it is already practicable to exploit the advantages of STEM microscopy of individual particles to define average three-dimensional distributions of mass in macromolecular complexes. This approach should be particularly useful for systems that for various reasons—e.g., paucity of material, impurity, polydispersity, fiber misalignment, or phase determination ambiguities—are refractory to diffraction analysis with x-rays or neutrons.

We gratefully acknowledge the skilled assistance of Ms. K. Cheung, Ms. M. Quandt, and Mr. F. Kito; generous provision of experimental materials by Dr. T. Schuster and Ms. M. Adams; and communication of x-ray results by Dr. G. Stubbs. We also thank Mrs. B. Morris for preparation of the manuscript.

1. Crewe, A. V. (1970) *Q. Rev. Biophys.* **3,** 137–175.
2. Lamvik, M. K. (1978) *J. Mol. Biol.* **122,** 55–68.
3. Wall, J. (1978) in *Introduction to Analytical Electron Microscopy*, eds. Hren, J. J., Goldstein, J. I. & Joy, D. C. (Plenum, New York), pp. 333–342.
4. Engel, A. (1983) *Micron* **13,** 425–436.
5. Caspar, D. L. D. (1956) *Nature (London)* **177,** 928.
6. Franklin, R. E. (1956) *Nature (London)* **177,** 928–930.
7. Mosesson, M. W., Hainfeld, J., Haschemeyer, R. H. & Wall, J. (1982) *J. Mol. Biol.* **153,** 695–718.
8. Paglini, S. & Lauffer, M. A. (1968) *Biochemistry* **7,** 1827–1835.
9. Scheele, R. B. & Schuster, T. M. (1975) *J. Mol. Biol.* **94,** 519–525.
10. Trus, B. L. & Steven, A. C. (1981) *Ultramicroscopy* **6,** 383–386.
11. Smith, P. R. (1978) *Ultramicroscopy* **3,** 153–160.
12. Knott, G. D. (1979) *Comp. Prog. Biomed.* **10,** 271–280.
13. Frank, J. (1980) in *Computer Processing of Electron Microscope Images*, ed. Hawkes, P. W. (Springer, Berlin), pp. 187–222.
14. Holmes, K. C. (1979) *J. Supramol. Struct.* **12,** 305–320.
15. Crowther, R. A. & Amos, L. A. (1971) *J. Mol. Biol.* **60,** 123–130.
16. Nonomura, Y. & Ohno, T. (1974) *J. Mol. Biol.* **90,** 523–527.